CFD Study of Subcooled Boiling Flow at Elevated Pressure Using a Mechanistic Wall Heat Partitioning Model

Machimontorn Promtong, Sherman C. P. Cheung, Guan H. Yeoh, Sara Vahaji, Jiyuan Tu

Abstract—The wide range of industrial applications involved with boiling flows promotes the necessity of establishing fundamental knowledge in boiling flow phenomena. For this purpose, a number of experimental and numerical researches have been performed to elucidate the underlying physics of this flow. In this paper, the improved wall boiling models, implemented on ANSYS CFX 14.5, were introduced to study subcooled boiling flow at elevated pressure. At the heated wall boundary, the Fractal model, Force balance approach and Mechanistic frequency model are given for predicting the nucleation site density, bubble departure diameter, and bubble departure frequency. The presented wall heat flux partitioning closures were modified to consider the influence of bubble sliding along the wall before the lift-off, which usually happens in the flow boiling. The simulation was performed based on the Two-fluid model, where the standard k-ω SST model was selected for turbulence modelling. Existing experimental data at around 5 bars were chosen to evaluate the accuracy of the presented mechanistic approach. The void fraction and Interfacial Area Concentration (IAC) are in good agreement with the experimental data. However, the predicted bubble velocity and Sauter Mean Diameter (SMD) are over-predicted. This over-prediction may be caused by consideration of only dispersed and spherical bubbles in the simulations. In the future work, the important physical mechanisms of bubbles, such as merging and shrinking during sliding on the heated wall will be incorporated into this mechanistic model to enhance its capability for a wider range of flow prediction.

Keywords—CFD, mechanistic model, subcooled boiling flow, two-fluid model.

I. Introduction

OPERATING the two-phase thermal systems such as nuclear reactors, boilers and heat exchangers requires a fundamental knowledge and in-depth understanding of the sophisticated heat and mass transfer processes occurring in subcooled boiling flows. Driven by the wide range of applications, the complex boiling mechanisms have been investigated intensively through experimental works [1]-[3]. These mechanisms include bubble growth, bubble lift-off at the heated surface and bubble condensation in bulk liquid, as well as the influence of the local fluid temperature, velocities of liquid and vapor, and bubble size distribution [4]-[8]. Basically, the size, the growth rate of vapor bubbles (frequency) and the waiting time during the bubble generation can represent the heat flux components [9]. They can also explain how quick the latent heat is transferred from the heated surface into the bulk liquid. Hence, these boiling parameters are generally involved in determining the wall heat flux partitions, including convective, quenching and evaporative heat fluxes [10], [11].

Over the past decades, a number of experimental works have studied the pool boiling and the flow boiling, which resulted in introducing many empirical correlations [10]-[14]. Consequently, these models have been adopted by Computational Fluid Dynamics (CFD) codes for predicting the nuclear system and boiling applications [15]-[17]. For instance, the RPI (*Rensselaer Polytechnic Institute*) model, which is available in ANSYS CFX is usually suitable for simulating pool boiling situation [18]. However, in order to predict the boiling flow, some researchers suggested that the constituted models have to be modified to account for more physical bubble behaviors, i.e. the bubble sliding and the condensation [19]-[22].

In this research, three constituted closures including Yu's fractal analysis [23], Klausner's force balance method [6] and Yeoh's mechanistic model [12], which are proposed to calculate the nucleation site density, bubble departure diameter and bubble frequency, respectively, are used for studying the subcooled boiling flow. In [24], it was shown that the predicted results using the proposed mechanistic wall partitioning model were in good agreement with low pressure experimental data. Recently, Ozar et al. investigated the sub-cooled boiling flow structure at elevated pressures [25], and this gives us an opportunity to assess the accuracy of our proposed mechanistic models by performing the validation study. Thus, the objectives of this paper are (i) to preliminarily investigate the possibility of this proposed mechanistic wall partitioning model in terms of predicting the local parameters (i.e. void fraction, SMD, liquid velocity, gas velocity) for the sub-cooled flow boiling when operating at high pressure (~5 bars), and also (ii) to elucidate some physical insights at the heated wall and over the fluid domain when specifying the Wet Steam (IAPWS-IF97) properties as the working fluid.

II. Sub-cooled Boiling Flow Phenomenon

A schematic showing the main characteristics of the sub-

Machimontorn Promtong is a PhD candidate in the School of Engineering, RMIT University, VIC 3083 Australia (corresponding author, phone: +61 (0) 42-364-5352, e-mail: s3466580@student.rmit.edu.au).

Sherman C.P. Cheung, Associate Professor, Sara Vahaji, Research fellow, Jiyuan Tu, Professor, are with the School of Engineering, RMIT University, VIC 3083 Australia (e-mail: chipok.cheung@rmit.edu.au, sara.vahaji@rmit.edu.au, jiyuan.tu@rmit.edu.au).

Guan H. Yeoh is a Professor in the school of Mechanical and Manufacturing Engineering, University of New South Wales, NSW 2052 Australia (e-mail: g.yeoh@unsw.edu.au).

cooled boiling flow is presented in Fig. 1. The sub-cooled liquid flow is introduced to the channel with heated wall, where vapor bubbles start to initiate at the surface of the heated wall at the ONB (Onset of Nucleate Boiling) point. The location, where the amount of vapor starts to significantly increase, is called as the Net Vapor Generation (NVG) point, in which the sub-cooling temperature is dominating the flow structure.

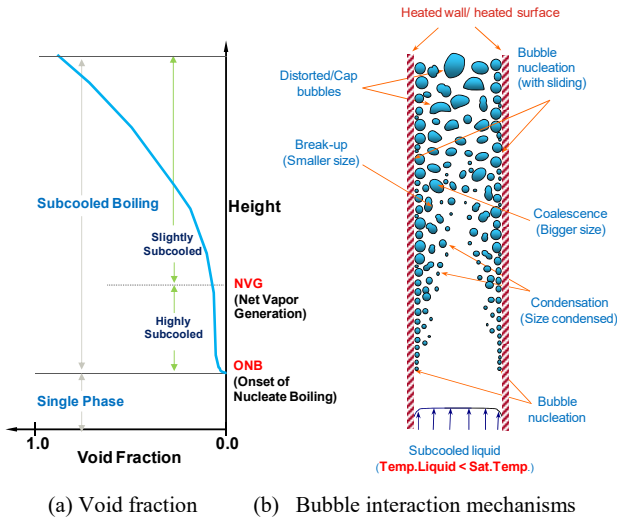(a) Void fraction   (b) Bubble interaction mechanisms

Fig. 1 Phenomenological descriptions of subcooled boiling flow

As shown on Fig. 1 (a), after the ONB point, the void fraction begins to increase along the wall height because of bubble generation and bubble interactions like the coalescence. On the other hand, the bubbles size might reduce or the bubbles might disappear because of break-up and condensation when they are exposed to the lower-temperature bulk liquid.

III. Modeling Equations

A. Two-Fluid Model

Physically, a sub-cooled boiling flow is described based on the averaged governing equations of continuity, momentum and energy for each phase. These equations of gas and liquid are solved separately for each individual phase, which can be represented as disperse phase (α_g) and continuum phase (α_l), respectively.

1. Continuity Equations

- *Gas Phase*

$$\frac{\partial \rho^g \alpha^g}{\partial t} + \nabla \cdot \left(\rho^g \alpha^g \bar{u}^g \right) = -\Gamma^{lg} \tag{1}$$

- *Liquid Phase*

$$\frac{\partial \rho^l \alpha^l}{\partial t} + \nabla \cdot \left(\rho^l \alpha^l \ \bar{u}^l \right) = \Gamma^{lg} \ ; \Gamma^{lg} = \frac{h^{lg} a^{if} (T_{sat} - T_l)}{h_{fg}} \tag{2}$$

where ρ is the density, α is the volume fraction, $\bar{u}$ is the

velocit vector. The term on the right hand side of (1) and (2) (Γ^{lg}) is involved in the calculation because of the condensation. The momentum equations of gas and liquid phases may be expressed as follows:

2. Momentum Equations

- *Gas Phase*

$$\frac{\partial \rho^g \alpha^g \bar{u}^g}{\partial t} + \nabla \cdot \left(\rho^g \alpha^g \bar{u}^g \bar{u}^g \right) = -\alpha^g \nabla P + \alpha^g \rho^g \bar{g}$$
$$+ \nabla \cdot \left[\alpha^g \mu_g^e \left(\nabla \bar{u}^g + \left(\nabla \bar{u}^g \right)^T \right) \right] - \Gamma^{lg} \bar{u}^g + F^{lg} \tag{3}$$

- *Liquid Phase*

$$\frac{\partial \rho^l \alpha^l \bar{u}^l}{\partial t} + \nabla \cdot \left(\rho^l \alpha^l \bar{u}^l \bar{u}^l \right) = -\alpha^l \nabla P + \alpha^l \rho^l \bar{g}$$
$$+ \nabla \cdot \left[\alpha^l \mu_l^e \left(\nabla \bar{u}^l + \left(\nabla \bar{u}^l \right)^T \right) \right] - \Gamma^{lg} \bar{u}^l + F^{lg} \tag{4}$$

where μ_l^e and μ_g^e are the effective viscosities of the liquid and gas phases, respectively. These viscosity terms are calculated using the turbulence models, in which their details are given as follows:

- *Turbulence Model*

Unlike single-phase fluid flow problem, some numerical investigations reveals that the Shear Stress Transport (SST) model, developed by Menter [26], is shown to provide more realistic prediction of gas volume fraction or void fraction close to the wall of the flow domain. Basically, this model applies the two-equation k-ω model near the wall and the two-equation k-ε model in the bulk flow. Therefore, the SST model is then introduced in this study. As shown in (5), effective viscosity (μ_e^l) for the continuous phase is a combination of the laminar (μ_{lam}^l), shear-induced turbulence (μ_{ts}^l) and Sato's bubble-induced turbulent viscosities (μ_{td}^l):

$$\mu_e^l = \mu_{lam}^l + \underbrace{\mu_{ts}^l + \mu_{td}^l}_{\mu_t^l} \tag{5}$$

For the shear-induced turbulence term, it can be given by:

$$\mu_{ts}^l = C_\mu \rho^l \left(k^l \right)^2 \big/ \varepsilon^l \tag{6}$$

Also, the bubble-induced turbulence can be calculated using:

$$\mu_{td}^l = C_{\mu p} \rho^l \alpha^g D_s \left| \mathbf{u}^g - \mathbf{u}^l \right| \tag{7}$$

The constants C_μ and $C_{\mu p}$ have values of 0.09 and 1.2 respectively. For the gas phase, the turbulent viscosity can be expressed by:

$$\mu_t^g = \frac{\rho^g}{\rho^l}\frac{\mu_t^l}{\sigma_g} \tag{8}$$

where σ_g is the turbulent Prandtl number of the gas phase which has a value of unity. The effective gas viscosity of the gas phase in (8) is subsequently determined as $\mu_e^g = \mu_{lam}^g + \mu_t^g$.

- Interfacial Momentum Forces

As shown in (3) and (4), the total interfacial force F^{lg} is required. This term is formulated based on different sub-forces affecting at the interface between both phases. Usually, in the simulation this interfacial force term is calculated by introducing the drag, lift, wall lubrication, and turbulent dispersion, which are shown in (9). More details regarding these terms can be found from [27].

The total interfacial force in (9) is given by $F^{gl} = -F^{lg}$ and due to drag force, the inter-phase momentum transfer between gas and liquid is given as:

$$F^{lg} = F_{drag}^{lg} + F_{lift}^{lg} + F_{lubrication}^{lg} + F_{dispersion}^{lg} \tag{9}$$

$$F_{drag}^{lg} = \frac{1}{8}C_D a_{if}\rho^l \left|\mathbf{u}^g - \mathbf{u}^l\right|\left(\mathbf{u}^g - \mathbf{u}^l\right) \tag{10}$$

From (10), the a_{if} term represents IAC. According to [28], the drag coefficient C_D in (10) has been formulated for several distinct Reynolds number regions for individual bubbles. For the lift force, it can be calculated based on the slip velocity and the curl of the liquid phase velocity as:

$$F_{lift}^{lg} = \alpha^g \rho^l C_L \left(\mathbf{u}^g - \mathbf{u}^l\right) \times \left(\nabla \times \mathbf{u}^l\right) \tag{11}$$

In (11), the constant C_L has been considered according to [29], which is calculated based on the function of Eotvos number (Eo). The proposed function could allow positive or negative lift coefficients. Usually, this would depend on the bubble size, the effects of bubble deformation and asymmetric wake of the bubble which is displayed as:

$$C_L = \begin{cases} \min\left[0.288\tanh\left(0.121Re_b\right), f\left(Eo_d\right)\right] & Eo < 4 \\ f\left(Eo_d\right) = 0.00105Eo_d^3 - 0.0159Eo_d^2 - 0.0204Eo_d + 0.474 & 4 \le Eo \le 10 \\ -0.29 & Eo > 10 \end{cases} \tag{12}$$

where the modified Eotvos number Eo_d can be calculated as:

$$Eo_d = \frac{g\left(\rho^l - \rho^g\right)D_H^2}{\sigma} \tag{13}$$

$$D_H = D_s \left(1 + 0.163Eo^{0.757}\right)^{1/3} \tag{14}$$

in which D_H is the maximum bubble horizontal dimension

that can be calculated by using the empirical correlation as [30]:

$$F_{lubrication}^{lg} = -\frac{\alpha^g \rho^l \left[\left(u^g - u^l\right) - \left(\left(u^g - u^l\right)n_w\right)\right]^2}{D_s}\left(C_{w1} + C_{w2}\frac{D_s}{y_w}\right)n_w \tag{15}$$

The wall lubrication force, which has a normal direction to the wall and decays with distance, can be expressed by:

$$F_{dispersion}^{lg} = -C_{TD}\left[\frac{1}{8}C_D a_{if}\rho^l \left|\mathbf{u}^g - \mathbf{u}^l\right|\right]\frac{\mu_t^g}{\rho^g Sc_b}\left(\frac{\nabla \alpha^g}{\alpha^g} - \frac{\nabla \alpha^l}{\alpha^l}\right) \tag{16}$$

where D_s is the Mean Sauter Bubble Diameter. Turbulence induced dispersion value is based on the Favre-averaging which was developed by [31]. The wall lubrication constants C_{w1} and C_{w2} in (15) are taken to have values of –0.0064 and 0.016 based on the suggestion by [32], where μ_t^g is the turbulent viscosity of the gas phase. In (16), the coefficient C_{TD} is set to a value of unity and S_{cb} (the turbulent bubble Schmidt number) has a value of 0.9.

3. Energy Equation

Because the gas phase is assumed to be at saturated situation, the calculating requirement of energy equation of gas phase can be ignored. The energy equation of liquid phase may be expressed as:

$$\frac{\partial \rho^l \alpha^l H^l}{\partial t} + \nabla \cdot \left(\rho^l \alpha^l \bar{u}^l H^l\right) = \nabla \cdot \left[\alpha^l \lambda_i^e \nabla T^l\right] + Q^{lg} + \left(\Gamma^{gl}H^l - \Gamma^{lg}H^l\right) \tag{17}$$

- Interfacial Energy Terms

Equation (18) expresses a calculation of the interfacial heat transfer (Q_g) term at the energy equation, which in this case represents the heat transfer due to the condensation process.

$$Q_{lg} = h_{lg}a_{if}(T_g - T_l); \; a_{if} = 6\alpha_g/D_s; \; D_s = \frac{1}{\sum_i \frac{f_i}{d_i}} \tag{18}$$

In order to calculate the heat transfer at the interface, the interfacial area term (a_{if}) is necessary, and as displayed in (18), it is calculated based on the bubble mean diameter (D_s) and gas void fraction (α_g).

B. Population Balance Method

Population Balance Methods (PBM) are widely applied to determine the coalescence and break-up phenomena of bubbles. In this simulation, Homogeneous Multiple-Size-Group (MUSIG) model, originally developed by Lo [33], was adopted to account a non-uniform bubble size distribution.

$$\frac{\partial \rho_j \alpha_j f_i}{\partial t} + \nabla \cdot \left(\rho_g \alpha_j f_i \bar{u}_j\right) = S_{j,i} - m_i(R_{ph})_i \tag{19}$$

where the source term ($S_{j,i}$) of this equation is a representative of the bubble birth and death rates. In detail, the interaction term $S_{j,i} = B_C + B_B - D_C - D_B$ contains the source rates of B_C, B_B, D_C and D_B, which are the birth rates due to coalescence (B_C) and break-up (B_D) and the death rates to coalescence (D_C) and break-up (D_B) of bubbles respectively. On a basis of the discrete approximation given in (19), the birth and death rates can be formulated according to:

$$B_C = \left(\rho_j^g \alpha_j^g\right)^2 \frac{1}{2} \sum_k \sum_l f_k f_l \frac{M_k + M_l}{M_k M_l} a(M_k, M_l) \tag{20}$$

$$D_C = \left(\rho_j^g \alpha_j^g\right)^2 \sum_k f_i f_k \frac{1}{M_k} a(M_i, M_k) \tag{21}$$

$$B_B = \rho_j^g \alpha_j^g \sum_k r(M_k, M_i) f_k \tag{22}$$

$$D_B = \rho_j^g \alpha_j^g f_i \sum_k r(M_i, M_k) \tag{23}$$

For the discretized contribution of the birth rate due to coalescence, it may be necessary to introduce the coalescence mass matrix as the fraction of mass due to coalescence between the kth bubble classes goes into the ith bubble classes. The coalescence mass matrix is defined as:

$$\eta_{kli} = \begin{cases} 1 & \text{if } M_k + M_l > M_i \\ 0 & \text{otherwise} \end{cases} \tag{24}$$

The birth rate due to coalescence is accordingly modified by multiplying the above matrix, η_{kli}, into (20). The coalescent rate and the break-up rate, proposed by Prince and Blanch [34] and Luo and Svendsen [35], are adopted for the PBM source term calculations. The second term on the right hand side of (19) represents the source rate due to the condensation.

C. The Proposed Mechanistic Models

In order to calculate the constituted parameters at the heat-flux partitioning algorithm, the proposed models which are adopted into the simulation are presented as follows:

1. Fractal Analysis

In this study, the fractal analysis, originally formulated by Mikic and Rosenow [36], is employed for the calculation of active nucleation site density. Considering a power correlation of the active cavities on the heated surface, the nucleation site density can be calculated. As shown in (25)-(28), the superheat (T_{sup}) and sub-cooling (T_{sub}) temperatures and other liquid properties such as thermal boundary layer thickness (δ_l), are mainly considered in this formulation.

$$N_a = \left(\frac{D_{c,max}}{D_c}\right)^{df} ; \quad D_{c,min} \le D_c \le D_{c,max} \tag{25}$$

$$D_{c,min} = 2\frac{\delta_l}{C_1}\left\{\frac{T_{sup}}{T_{sub}} - \sqrt{\left[\frac{T_{sup}}{T_{sub}}\right]^2 - \frac{4\zeta C_3}{\delta(T_{sup})}}\right\} \tag{26}$$

$$D_{c,max} = 2\frac{\delta_l}{C_1}\left\{\frac{T_{sup}}{T_{sub}} + \sqrt{\left[\frac{T_{sup}}{T_{sub}}\right]^2 - \frac{4\zeta C_3}{\delta(T_{sup})}}\right\} \tag{27}$$

$$d_f = \frac{\ln\left[\frac{1}{2}\left(\frac{\overline{D}_{c,max}}{D_{c,min}}\right)^2\right]}{\ln\frac{D_{c,max}}{D_{c,min}}} \tag{28}$$

From the above equations, $D_{c,max}$ and $D_{c,min}$ are the maximum and minimum of active cavity diameter. The d_f term represents the area fractal dimension ($1 < d_f < 2$) and Φ is the contact angle of the fluid on the heated wall. The other terms can be calculated as $C_1 = (1 + \cos\Phi)/\sin\Phi$, $C_3 = 1 + \cos\Phi$, and $\zeta = 2\sigma T_{sat}/\rho_g h_{fg}$. Further details regarding the fractal analysis can be found in [23].

2. Force Balance Approach

The force balance approach, formulated by [6] and [37], is introduced for calculating the bubble lift-off diameter. All the forces acting on the vapor bubbles are depicted in Fig. 2, and the equations used for calculating the bubble diameter are shown in (29) and (30).
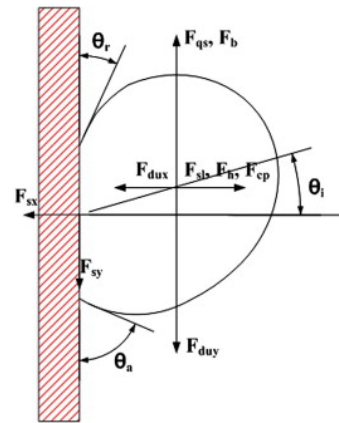

Fig. 2 Forces acting on a vapor bubble before leaving the heated wall [21]

- Along the x-direction:

$$\sum F_x = F_{sx} + F_{dux} + F_{sL} + F_h + F_{cp} \tag{29}$$

$$F_{sx} = -d_w \sigma \frac{\pi}{\theta_a - \theta_r} [\cos \theta_r - \cos \theta_a]; \ F_{dux} = -F_{du} \cos \theta_i$$

$$F_{sL} = \frac{1}{2} C_L \rho_l \Delta U^2 \pi r^2; \ F_h = \frac{9}{4} \rho_l \Delta U^2 \frac{\pi d_w^2}{4}; \ F_{cp} = \frac{\pi d_w^2}{4} \frac{2\sigma}{r_r}$$

- Along the y-direction:

$$\sum F_y = F_{sy} + F_{duy} + F_{qs} + F_b \qquad (30)$$

$$F_{sy} = -d_w \sigma \frac{\pi(\theta_a - \theta_r)}{\pi^2 - (\theta_a - \theta_r)^2} [\sin \theta_a + \sin \theta_r]; \ F_{duy} = -F_{du} \sin \theta_i$$

$$F_{qs} = 6C_D \mu_l \Delta U \pi r; \ F_b = \frac{4}{3} \pi r^3 (\rho_l - \rho_g) g$$

where F_{sx}, F_{sy} are the surface tension forces; F_{dux}, F_{duy} are the unsteady drag forces due to asymmetrical growth of the bubble; F_{sL} is the shear lift force; F_h is the force due to the hydrodynamic pressure. Also, F_{cp} is the contact pressure force, F_{qs} is the quasi steady-drag force in the flow direction, and F_b is the buoyancy force. Also, θ_a, θ_r and θ_i are the advancing, receding and inclination angles, respectively; d_w is surface/bubble contact diameter; g is gravitational acceleration; r is the bubble radius and ΔU is the relative velocity between bubble and the liquid; C_D and C_L are drag and lift force coefficients, respectively whose formula could be found in Klausner's work [6].

The bubble lift-off diameter (D_l) can be gained when a summation of the forces involved in perpendicular direction to the wall is equal to zero $\left(\sum F_x = 0 \right)$. Similarly, for the y-direction, several forces are involved in calculating the size of the sliding bubble (D_{sl}). This sliding diameter can be obtained when the summation of forces reaches zero $\left(\sum F_y = 0 \right)$. This diameter is required for the calculation of the bubble influence area in the quenching heat flux term.

3. Mechanistic Frequency Model

In order to calculate the bubble departure frequency, the mechanistic model proposed by Yeoh et al. [12] is adopted. At the active cavity site, the total time required for each vapor bubble generation (its life cycle) can be calculated by combining the waiting time and the growth time. This formula for the bubble lift-off frequency can be seen from (31):

$$f = \frac{1}{t_w + t_g} \qquad (31)$$

$$t_w = \frac{1}{\pi \eta} \left[\frac{(T_{sup} + T_{sub}) C_1 r_c}{T_{sup} + 2\sigma T_{sat} / C_2 \rho_g h_{fg} r_c} \right]^2 \qquad (32)$$

$$t_g = \frac{1}{16} \frac{\pi}{\eta} \frac{D_{sl}^2}{b^2 Ja^2}; \ Ja = \left(\frac{\rho_l k_l T_{sup}}{\rho_g h_{fg}} \right) \qquad (33)$$

The consuming time after the departure of a vapor bubble from the cavity site and just before the regeneration of a new vapor bubble (waiting or quenching time) can be estimated by using Hsu's criteria (32). From (32), T_{sup} is the wall superheat and T_{sub} is the sub-cooled temperature. The two constant terms can be calculated using the following equations $C_1 = (1 + \cos \theta) / \sin \theta$, $C_2 = 1 / \sin \theta$. Moreover, r_c is the cavity radius and η is the liquid thermal diffusivity.

Further details regarding the equations can be found in [12]. The growth time (t_g) can be obtained by substituting the sliding diameter (D_{sl}) into (33), where Ja is the Jacob number.

IV. EXPERIMENTAL DETAILS

According to Ozar's experimental works which observed the subcooled boiling flow at elevated pressure, usually two bubble groups including spherical and distorted bubbles (Group-1) and cap, slug and churn-turbulent bubbles (Group-2) can be observed [25]. In this validation study, two cases from his experiments are selected to assess the prediction accuracy of the current mechanistic model. Their operation details are presented in Table I. Working fluid used in the experiments was sub-cooled water.

The uncertainties of the void fraction, liquid and gas velocities were mentioned to be <10%, ±0.75% and <10%, respectively. For the temperature and pressure, they were at ±2.2 K and <± 0.50%, respectively.

TABLE I
OPERATING CONDITIONS OF THE SELECTED EXPERIMENTAL CASES

Case	Qwall (kW/m²)	P_{inlet} (kPa)	Inlet Velocity (m/s)	Subcooling Temp. (K)
OZAR191	190.9	497	1.03	14.8
OZAR241	240.8	504	1.02	14.9

As can be seen from Fig. 3, the experimental configuration consisted of a vertical concentric annulus with an inner heating rod of 19.1 mm outer diameter. The diameter of outer wall is 38.1 mm. The lengths of heated section and unheated section were 2.845 m and 1.632 m, respectively. This rod could produce a uniform maximum heat flux of 260 kW/m². From the figure, totally, there are five measuring elevations of local radial parameters at the test section; three locations at the heated section (L/D_h =51.6, 108, 149) and two locations at the adiabatic section (L/D_h =189, 230).

V. SIMULATION DESCRIPTIONS

Basically, two sets of the continuity equation, momentum equations of each phase and one energy equation of liquid phase were simultaneously solved based on the Finite Volume Method (FVM). The Semi Implicit (SIMPLE) algorithm was used to handle the coupling of velocity-pressure calculation [38]. To track the bubble size distribution, the PBM (Homogenous MUSIG) was employed; therefore, 15 extra transport equations were iteratively coupled with the flow

equations [39]. These bubble groups were equally divided for bubble sizes between 0 mm and 8.5 mm.
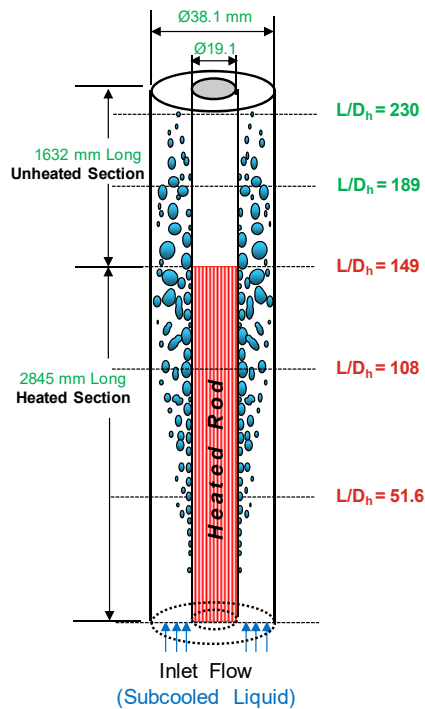

Fig. 3 A schematic of the measuring locations for the local parameters of Ozar's experiments

Because the geometry has an annular shape, thus only a quarter of the annulus could be used for this simulation. The total mesh was 5400, with 10 (radial) x 180 (height) x 3 (circumference). Wall heat fluxes, mass fluxes, and sub-cooling temperatures from the experiments were adopted as the boundary and initial conditions. Moreover, to gain a realistic simulation, the Wet Steam (IAPWS-IF97) properties at the considered flow ranges were adopted as the working fluid. For the turbulent models, the k–ω SST model was adopted for the liquid phase and dispersed phase zero-equation was employed for the gas phase.

In the simulation, the fractal model [13], the force balance method [9], and the mechanistic model [1], were implemented into the ANSYS CFX 14.5 (via the user FORTRAN files)). For each equation of the size fraction, additional source terms have been adopted to include the condensation effect. Also, at the heated wall, the nucleation terms were adopted at the size group equations, which have the mean diameter close to the lift-off diameter as the evaporative heat sources. The convergence of all the cases was observed below 1×10^{-5}.

VI. RESULTS AND DISCUSSIONS

In this validation study, the predictions of local mean radial profiles of void fraction, IAC, Saunter Mean Diameter and bubble velocity for all the cases at different measuring locations within the heated section (L/D_h = 51.6, 108 and 149) are particularly compared with the experimental data.

Noticeably, the difference between those two selected cases is the heat supplying rates at the heated wall (190.9 kW/m^2 and 240.8 kW/m^2). Physically, this alteration could result in a different number of bubbles nucleated on the heated surface. As a consequence, a high population of vapor bubbles may appear near the wall. Once their sizes become sufficiently large because of the coalescence interaction, they possibly move to the center of the annulus. Eventually, this situation may lead to an occurrence of Group-2 bubbles (i.e. cap and slug bubbles).

A. Local Flow Structure

1. Void Fraction (ε)

In the flow region at the heated section, the void fraction is increased along the heated wall (Figs. 4 (a) and 5 (a)). The peak of void fraction may be caused due to nucleation of many bubbles at the heated surface. In general, when the bubbles depart from the heated surface and are exposed to the subcooled liquid, the bubbles get condensed. Hence, the void fractions are decreased in the radial direction away from the wall and gradually become zero at the far region. For both cases, it could be seen that the void fraction at L/D_h = 51.6 is nearly zero. This means that there are almost zero of bubbles nucleated at around this region. Clearly, the resultant void fraction at the mid-way of heated section (L/D_h = 108) and at the last region before unheated zone (L/D_h = 149) are in very good agreement with the experimental data except the region near the heated wall. This could be an outcome of an accurate prediction of the evaporative heat portion at the heated wall. Among those three locations for a relatively low heat flux case (Q_{wall} = 190 kW/m^2), only Group-1 bubbles exist. At near the exit of heated section, the maximum void fraction (~ 0.30) is found. Moreover, away from the heated wall in the radial direction, lower void fractions compared to the experimental data are observed. This discrepancy could be the result of a low estimated rate of bubble coalescence and/or a high predicted rate of bubble breakage in the simulation whose interactions are currently assumed only for spherical bubbles.

The effect of wall heat flux can be clearly observed from Fig. 5 (a) (Q_{wall} = 241 kW/m^2, L/D_h = 149) as the Group-2 bubbles are found. Possibly, at this operating condition, it may cause an occurrence of low local subcooling temperature and high bubble density at near the end of heated region, consequently big bubbles (Group-2) can be triggered by the coalescence mechanism.

Currently, we are only considering dispersed and spherical bubbles (Group-1) in our simulation. Interestingly, Fig. 5 (a) (L/D_h = 149) shows that the predicted void fraction is found in a good agreement with the experimental results which represent a summation of Group-1 and Group-2. Therefore, this prediction can be introduced for capturing the change of void fraction along the heated subcooled region.

2. Interfacial Area Concentration (IAC)

Figs. 4 (b) and Fig. 5 (b) show the local radial profiles of predicted IAC compared with the existing experimental data. Similar to void fraction profiles, the highest IAC is found near

the heated wall for both cases.

For low heat flux case (Q_{wall} = 190 kW/m^2), because of low bubble density, only Group-1 bubbles influence the overall IAC value. As shown in Fig. 4 (b), the predicted IAC agrees well with the experimental data except near the inlet, which is slightly higher. Moreover, at L/D_h = 149, the highest value for IAC is found around 800-1000 m^{-1} near the heated surface. Also, the IAC value reduces to zero at far region as a result of the condensation which usually causes a collapse of bubbles.

For higher heat flux case (Fig. 5 (b)), the IAC of Group-2 bubbles is started to be noticed at L/D_h = 149. The high IAC is found near the heated wall, which may be caused by a high population of small bubbles. Because of bubble merging while sliding on the heated wall, then the Group-2 bubbles can be formed at this region and its IAC value represents at high number as well. In this prediction, the value of IAC at near the end of heated zone (L/D_h = 149) is attempted to be compared with a summation of the experimental IAC values of Group-1 and Group-2. Overall, at the heated subcooled region, the predicted IAC is in good agreement with the experimental data.

3. Sauter Mean Diameter (SMD)

The comparisons of SMD between the predictions and the experiments are shown in Figs. 4 (c) and 5 (c). Normally, after leaving the heated wall, the bubbles can merge with the neighbouring bubbles and/or break up because of random collisions and turbulent impact, which could result in the change of their sizes. At the same time, in the radial direction away from the heated wall, the bubble diameter can get smaller or even disappear because of condensation.

As we know, normally the lift and wall forces make the small bubbles (Group-1) staying near the wall, whereas the bigger bubbles (Group-2) are moved to the center of the annulus. Since there is low turbulent kinetic energy (less shearing-off situation) at the center, the Group-2 bubbles can increase the size further because of random collision and wave entrainment.

To avoid the numerical instability problems, unlike experiments, usually the minimum bubble size in the numerical prediction cannot set to be zero. Nevertheless, the possible smallest size in the numerical simulation could be equal to the smallest bubble group size. As presented in Figs. 4 (c) and 5 (c), the predicted bubble size is found to be similar with the smallest bubble size group (~1.1-1.3 mm) at the first measuring location at the heated section (L/D_h = 51.6). This explains the discrepancy between the experimental data, which is equal to zero due to having no bubbles at this location, and the numerical predictions.

As shown in Fig. 4 (c), the bubble diameters are increased following the flow downstream due to the coalescence mechanisms. At L/D_h = 108, the predicted SMD is quite similar in size compared to the experimental data at near the heated wall. However, at the far region, this predicted diameter is higher than that observed in the experiment (Fig. 4 (c)). This could be a result of the lift-force coefficient calculation. At the present work, the Tomiyama's model is adopted, in which the small bubbles (< ~5.0 mm) are normally pushed to both sides of the wall. Thus, higher prediction of the SMD at far region from the heated wall may be occurred.

For the SMD at L/D_h = 149, a similarity of the peak location between the prediction and the experiment could be noticed and the biggest size can be found at the middle of the annulus gap. However, the SMD from the numerical predictions for both cases are smaller than that observed in the experiment. An assessment of the available lift-force coefficient models may be useful.
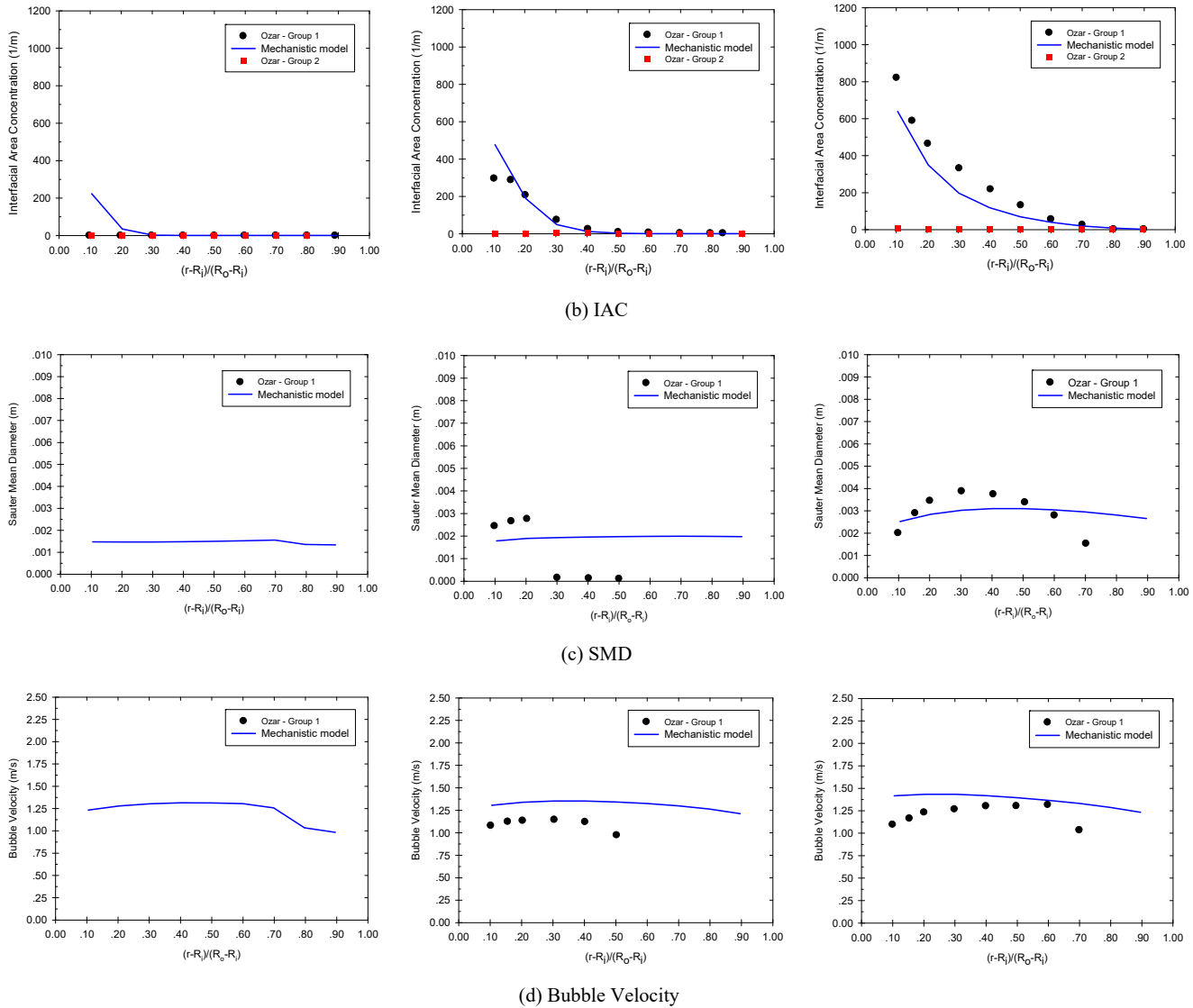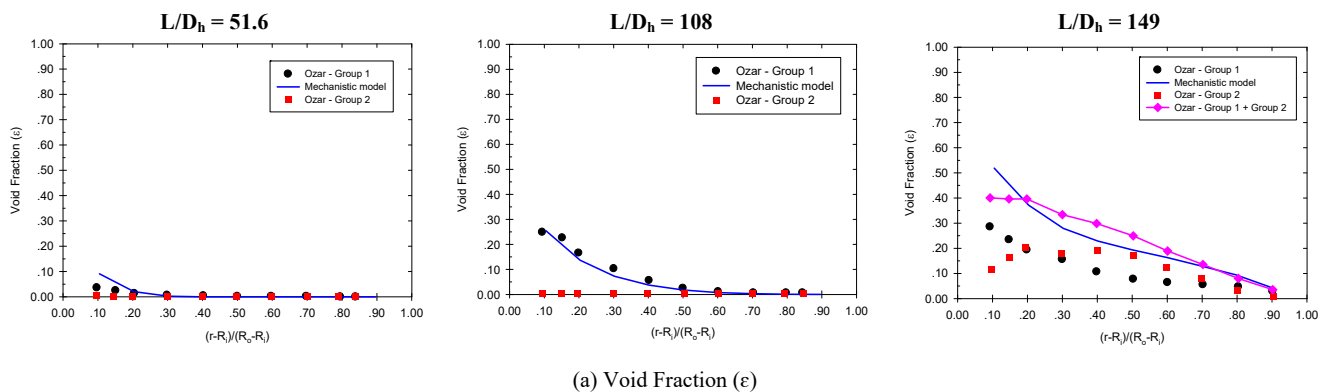

(a) Void Fraction (ε)

(b) IAC

(c) SMD

(d) Bubble Velocity
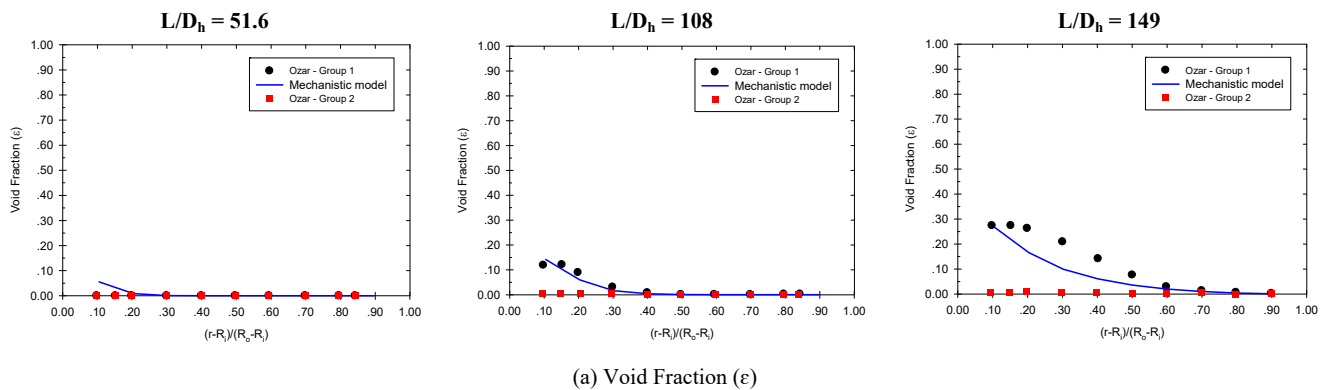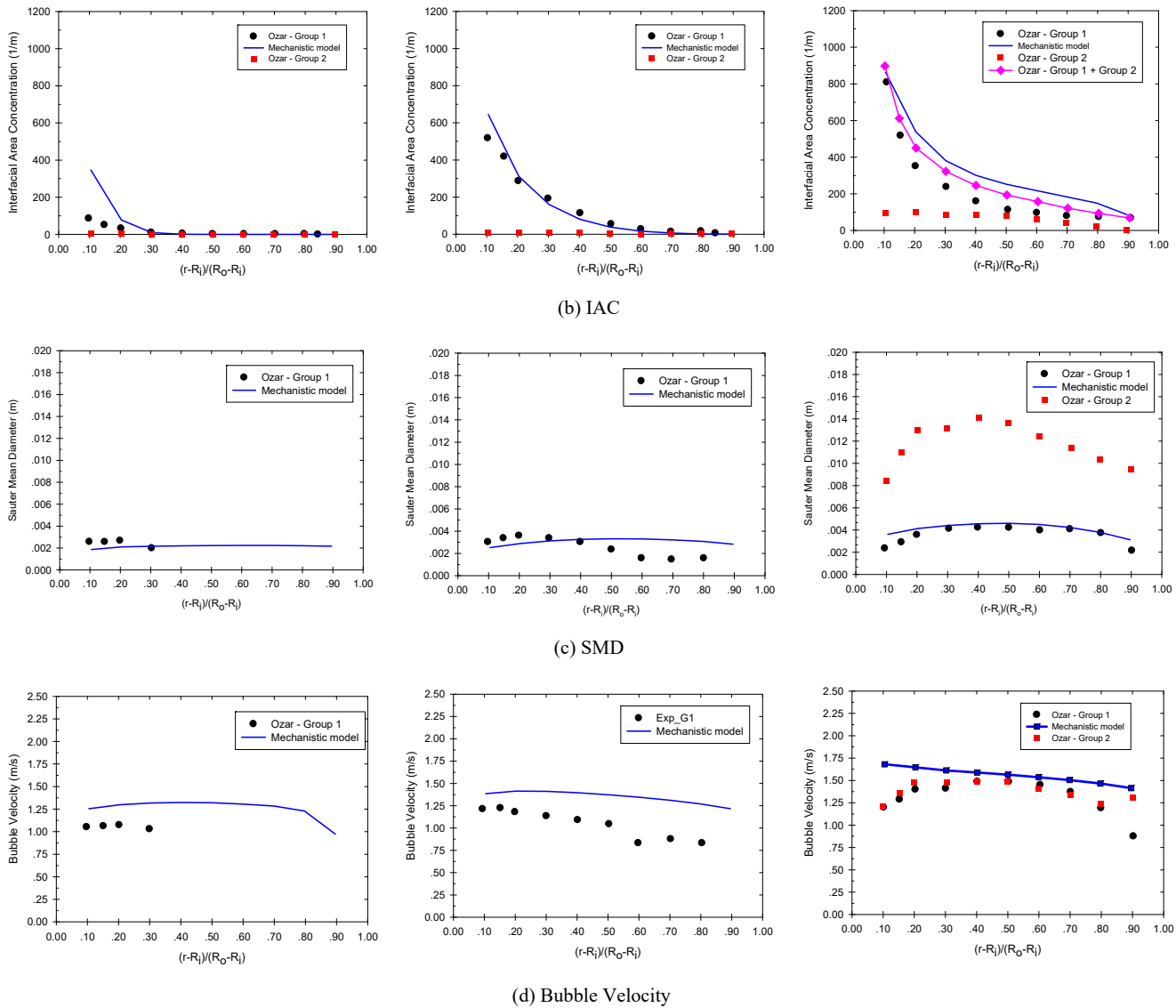
Fig. 4 Comparisons of local radial profiles of the considered parameters between the predictions the experiments for OZAR191
(Q_{wall} = 191 kW/m^2, V_{inlet} = 1.03m/s, T_{sub} = 14.8 K, P_{inlet}=498 kPa)

L/D$_h$ = 51.6   **L/D$_h$ = 108**   **L/D$_h$ = 149**

(a) Void Fraction (ε)

(b) IAC

(c) SMD

(d) Bubble Velocity

Fig. 5 Comparisons of local radial profiles of the considered parameters between the predictions the experiments for OZAR241
(Q_{wall} = 241 kW/m², V_{inlet} = 1.02m/s, T_{sub} = 14.9 K, P_{inlet}=504 kPa)

4. Bubble Velocity

The local radial profiles of bubble velocities are shown in Figs. 4 (d) and 5 (d). From the experimental data, the bubble velocity at L/D_h = 51.6 is equal to zero since no bubble has been generated yet. However, as mentioned earlier, in the numerical predictions, the size of the bubble cannot be equal to zero. Therefore, there is a bubble velocity shown on the figure whose normally may be equal to the liquid velocity.

For the other elevations (L/D_h = 108 and L/D_h = 149), the predicted velocities at near the heated wall are higher than the experimental results. This could be caused by the smaller predicted sizes of bubbles on that area than the experiments, which could result in higher predicted velocities. Nevertheless, in the reality, while the vapor bubbles flow up, they may merge/collide to the neighboring bubbles that are still attached to the heated rod. These may become bigger bubbles and would also be resulted in lower bubble velocities at the region near the heated rod. As mentioned earlier, using the Tomiyama's lift-coefficient model [29] in the simulation, it may enhance an occurrence of small bubbles near the unheated wall as well. Hence, currently the bubble velocities close to that adiabatic surface are also found to be higher than the experimental results.

B. Other Simulation Results near Heated Wall

The subcooling temperature and the void fraction profiles near the heat wall for the case of higher heat flux (OZAR241) are provided in Fig. 6. Precisely, the values of these parameters were obtained from the first nodes from the heated wall along the height of the annulus.
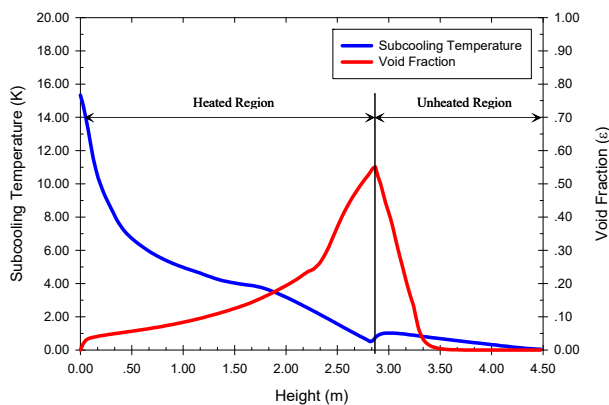
Fig. 6 The subcooling temperature and the void fraction collecting near the heat wall along the height

As shown, the bulk liquid has the subcooling temperature at around 15 K at the inlet, and then the liquid removes the heat from the wall and gradually becomes a slight subcooling liquid near the end of the heated section. At around 2.8 m of the height, the subcooling temperatures near the heated wall reduce to a small number (~1-2 K). Actually at this value, the bubble generation rate could be high and Group-2 bubbles could form due to high density of the vapor bubbles. However, if the heat flux is not sufficient, this kind of situation (formation of large bubbles) may not be occurred.

It is clearly seen that the void fraction near the heated wall increases and reaches around 0.6 at near the exit of the heated region. The point of intersection between the subcooling temperature and void fraction profiles might be the NGV point. This is because the subcooling temperature becomes more stable at this region. Also, a rapid increase of the void fraction is found beyond this location, which could confirm the occurrence of NVG.

VII. CONCLUSION AND FUTURE WORKS

The improved models of the wall flux heat partition algorithm including the fractal analysis, the force balance method, and the mechanistic bubble departure frequency, are successfully implemented into the ANSYS CFX 14.5 for studying the local parameters of the sub-cooled boiling flow when operating at elevated pressure. By using the Wet Steam (IAPWS-IF97) as the working fluid, some realistic mechanisms of the sub-cooled boiling flow are noticed, for instance, the NVG point could be observed.

In this validation study, the prediction results including the void fraction and IAC are in very good agreement with the experimental data. Hence, by using this mechanistic approach, the evaporative heat flux could be estimated appropriately for the current heat and mass conditions. Also, the prediction of the other parameters including Bubble SMD, and bubble velocity are found in satisfactory agreement with the experimental data.

For the future work, our attentions will be directly toward the assessment of the available lift-coefficient models especially for the subcooled boiling flow. Hopefully, this way could give a better capture of the bubble size distribution. Introducing this mechanistic model to investigate at more number of flow conditions is also necessary. To extend the current mechanistic model for predicting the subcooled boiling flow for a wider range of flow operations, the development of the force balance method, i.e. the micro-layer evaporation, the condensation at the bubble tips and bubble merging during sliding, will be particularly focused as well.

REFERENCES

[1] Zeitoun, O. and M. Shoukri, *Axial Void Fraction Profile in Low Pressure Subcooled Flow Boiling.* 1996.
[2] Lee, T.H., G.C. Park, and D.J. Lee, *Local flow characteristics of subcooled boiling flow of water in a vertical concentric annulus.* International Journal of Multiphase Flow, 2002. 28(8): p. 1351-1368.
[3] Situ, R., et al., *Flow structure of subcooled boiling flow in an internally heated annulus.* International Journal of Heat and Mass Transfer, 2004. 47(24): p. 5351-5364.
[4] Zuber, N., *The Dynamics of Vapor Bubbles in Nonuniform Temperature Fields.* International Journal of Heat and Mass Transfer, 1961. 2: p. 83-98.
[5] Zeitoun, O. and M. Shoukri, *Bubble behavior and mean diameter in subcooled flow boiling.* Journal of Heat Transfer-Transactions of the Asme, 1996. 118(1): p. 110-116.
[6] Klausner, J.F., et al., *Vapor Bubble Departure in Forced-Convection Boiling.* International Journal of Heat and Mass Transfer, 1993. 36(3): p. 651-662.
[7] Situ, R., et al., *Photographic study of bubble behaviors in forced convection subcooled boiling.* International Journal of Heat and Mass Transfer, 2004. 47(17-18): p. 3659-3667.
[8] Thorncroft, G.E., J.F. Klausner, and R. Mei, *An experimental investigation of bubble growth and detachment in vertical upflow and downflow boiling.* International Journal of Heat and Mass Transfer, 1998. 41(23): p. 3857-3871.
[9] Situ, R., et al., *Bubble departure frequency in forced convective subcooled boiling flow.* International Journal of Heat and Mass Transfer, 2008. 51(25-26): p. 6268-6282.
[10] Basu, N., G.R. Warrier, and V.K. Dhir, *Wall Heat Flux Partitioning During Subcooled Flow Boiling: Part 1—Model Development.* Journal of Heat Transfer, 2005. 127(2): p. 131.
[11] Warrier, G.R. and V.K. Dhir, *Heat Transfer and Wall Heat Flux Partitioning During Subcooled Flow Nucleate Boiling—A Review.* Journal of Heat Transfer, 2006. 128(12): p. 1243.
[12] Yeoh, G.H., et al., *Fundamental consideration of wall heat partition of vertical subcooled boiling flows.* International Journal of Heat and Mass Transfer, 2008. 51(15-16): p. 3840-3853.
[13] Cheung, S.C.P., et al., *Modeling subcooled flow boiling in vertical channels at low pressures – Part 1: Assessment of empirical correlations.* International Journal of Heat and Mass Transfer, 2014. 75: p. 736-753.
[14] Basu, N., G.R. Warrier, and V.K. Dhir, *Onset of Nucleate Boiling and Active Nucleation Site Density during Subcooled Flow Boiling.* Journal of Heat Transfer, 2002. 124(4): p. 717-728.
[15] Tu, J.Y. and G.H. Yeoh, *On numerical modelling of low-pressure subcooled boiling flows.* International Journal of Heat and Mass Transfer, 2002. 45(6): p. 1197-1209.
[16] Yeoh, G.H. and J.Y. Tu, *A unified model considering force balances for departing vapour bubbles and population balance in subcooled boiling flow.* Nuclear Engineering and Design, 2005. 235(10-12): p. 1251-1265.
[17] Kocamustafaogullari, G. and M. Ishii, *Interfacial Area and Nucleation Site Density in Boiling Systems.* International Journal of Heat and Mass Transfer, 1983. 26(9): p. 1377-1387.

[18] Kurul, N.a.P., M. Z., *On the modeling of multidimensional effects in boiling channels.* ANS Proc. 27th National Heat Transfer Conference, Minneapolis, MN, 1991.

[19] Yeoh, G.H., et al., *Modeling subcooled flow boiling in vertical channels at low pressures – Part 2: Evaluation of mechanistic approach.* International Journal of Heat and Mass Transfer, 2014. 75: p. 754-768.

[20] Situ, R., et al., *Bubble lift-off size in forced convective subcooled boiling flow.* International Journal of Heat and Mass Transfer, 2005. 48(25-26): p. 5536-5548.

[21] Cho, Y.-J., et al., *Development of bubble departure and lift-off diameter models in low heat flux and low flow velocity conditions.* International Journal of Heat and Mass Transfer, 2011. 54(15-16): p. 3234-3244.

[22] Xu, J., et al., *Experimental visualization of sliding bubble dynamics in a vertical narrow rectangular channel.* Nuclear Engineering and Design, 2013. 261: p. 156-164.

[23] Yu, B. and P. Cheng, *A Fractal Model for Nucleate Pool Boiling Heat Transfer.* Journal of Heat Transfer, 2002. 124(6): p. 1117.

[24] Promtong, M., S.C.P. Cheung, and J. Tu. *Numerical modelling of subcooled boiling flow based on mechanistic approach: A validation study using wet steam (IAPWS) as working fluid properties.* in *Lecture Notes in Engineering and Computer Science.* 2016.

[25] Ozar, B., et al., *Interfacial area transport of vertical upward steam–water two-phase flow in an annular channel at elevated pressures.* International Journal of Heat and Mass Transfer, 2013. 57(2): p. 504-518.

[26] Menter, F.R., *2-Equation eddy-visocity turbulence models for engineering applications.* Aiaa Journal, 1994. 32(8): p. 1598-1605.

[27] Anglart, H. and O. Nylund, *CFD application to prediction of void distribution in two-phase bubbly flows in rod bundles.* Nuclear Engineering and Design, 1996. 163(1–2): p. 81-98.

[28] Ishii, M. and N. Zuber, *Drag Coefficient and Relative Velocity in Bubbly, Droplet or Particulate Flows.* Aiche Journal, 1979. 25(5): p. 843-855.

[29] Tomiyama, A., *Struggle with computational bubble dynamics*, in *Third International Conference on Multiphase Flow.* 1998: Lyon, France 157.

[30] Wellek, R.M., A.K. Agrawal, and A.H. Skelland, *Shape of liquid drops moving in liquid media.* Aiche Journal, 1966. 12(5): p. 854-&.

[31] Burns, A.D., et al. *The Farve averaged drag model for turbulent dispersion in Eulerian Mulit-phase flows.* in *Proceeding of the Fifth International Conference on Multiphase flow.* 2004.

[32] Krepper, E., D. Lucas, and H.M. Prasser, *On the modelling of bubbly flow in vertical pipes.* Nuclear Engineering and Design, 2005. 235(5): p. 597-611.

[33] Lo, S. and A. Technology, *Application of Population Balance to CFD Modeling of Bubbly Flow Via the MUSIG Model.* 1996.

[34] Prince, M.J. and H.W. Blanch, *Bubble coalescence and break-up in air-sparged bubble columns.* AIChE Journal, 1990. 36(10): p. 1485-1499.

[35] Luo, H. and H.F. Svendsen, *Theoretical model for drop and bubble breakup in turbulent dispersions.* AIChE Journal, 1996. 42(5): p. 1225-1233.

[36] Mikic, B.B. and W.M. Rosenow, *A new correlation of pool-boiling data including the effect of heating surface characteristics.* Journal of Heat Transfer, 1969.

[37] Zeng, L.Z., et al., *A unified model for the prediction of bubble detachment diameters in boiling systems—II. Flow boiling.* International Journal of Heat and Mass Transfer, 1993. 36(9): p. 2271-2279.

[38] Patankar, S., *Numerical heat transfer and fluid flow.* 1980: CRC press.

[39] Yeoh, G.H., C.P. Cheung, and J. Tu, *Chapter 3 - Population Balance Approach—A Generic Framework*, in *Multiphase Flow Analysis Using Population Balance Modeling.* 2014, Butterworth-Heinemann: Oxford. p. 69-90.